



Wave-frequency flows within a near-bed vegetation canopy



Stephen M. Henderson^{a,*}, Benjamin K. Norris^b, Julia C. Mullarney^b, Karin R. Bryan^b

^a School of the Environment, Washington State University (Vancouver), Vancouver, WA 98686, USA

^b Coastal Marine Group, Faculty of Science and Engineering, University of Waikato, Hamilton 3240, New Zealand

ARTICLE INFO

Keywords:

Wave dissipation
Drag coefficient
Mangrove
Photogrammetry
Estuaries
Vegetation

ABSTRACT

We study water flows and wave dissipation within near-bed pneumatophore canopies at the wave-exposed fringe of a mangrove forest on Cù Lao Dung Island, in the Mekong Delta. To evaluate canopy drag, the three-dimensional geometry of pneumatophore stems growing upward from the buried lateral roots of *Sonneratia caseolaris* mangroves was reconstructed from photogrammetric surveys. In cases where hydrodynamic measurements were obtained, up to 84 stems per square meter were observed, with stem heights < 0.6 m, and basal diameters 0.01–0.02 m. The parameter $a =$ (frontal area of pneumatophores blocking the flow)/(canopy volume) ranged from zero to 1.8 m^{-1} . Within-canopy water velocity displayed a phase lead and slight attenuation relative to above-canopy flows. The phase lead was frequency-dependent, ranging from 0 to 30 degrees at the frequencies of energetic waves (> 0.1 Hz), and up to 90 degrees at lower frequencies. A model is developed for wave-induced flows within the vertically variable canopy. Scaling suggests that acceleration-induced forces and vertical mixing were negligible at wave frequencies. Consistent with theory, drag-induced vertical variability in velocity scaled with $\Lambda = T_w/(2\pi T_f)$, where $T_w =$ wave period, $T_f = 2/(C_D a |u|)$ is the frictional time scale, $C_D \approx 2$ is the drag coefficient, and $|u|$ is a typical flow speed. For fixed wave conditions ($|u|$ and T_w), theory predicts increasing dissipation with increasing vegetation density (i.e. increasing a), until a maximum is reached for order-one Λ . For larger Λ , within-canopy flow is so inhibited by drag that further increases in a reduce within-canopy dissipation. For observed cases, $\Lambda \leq 0.38$ at energetic wave frequencies, so wave dissipation near the forest edge is expected to increase with increasing pneumatophore canopy density. However, under different wave conditions, the most dense canopies may occasionally approach the dissipation maximum ($\Lambda \approx 1$). Predicted dissipation by the pneumatophore canopy was sufficient to attenuate most wave energy over distances slightly less (more) than 100 m into the marsh in 1 m (2 m) water depth.

1. Introduction

Aquatic vegetation can shelter coastlines from energetic waves and currents (Riffe et al., 2011; Jadhav et al., 2013; Temmerman et al., 2013), and sometimes creates low-energy regions of sediment deposition (Furukawa et al., 1997; Bouma et al., 2007). Diverse coastal wetland ecosystems (Greenberg et al., 2006) are often productive regions of rapid carbon burial (Siikamäki et al., 2012), and many wetlands are threatened by pollution, land reclamation, and conversion to aquaculture. Mangrove forests, in particular, have been impacted by widespread deforestation (Thu and Populus, 2007; Giri et al., 2011). In Vietnam's Mekong Delta, reduced sediment supply is expected to compound the effects of rising sea levels on coastal evolution (Anthony et al., 2015; Nicholls et al., 1999). Improved understanding of interacting hydrodynamics and morphodynamics may prove relevant to prediction of coastal flooding or erosion, and to management of mangrove ecosystems,.

We present observations from a mangrove-covered coast in the southern Mekong Delta. This coast is exposed to the open ocean, and therefore to energetic waves. Previous researchers have measured attenuation of waves propagating into mangrove forests, finding substantial dissipation after tens or hundreds of meters of propagation (Mazda et al., 2006; Bao, 2011; Horstman et al., 2014). A variety of models have been developed to predict wave dissipation within vegetation. Dalrymple et al. (1984) modeled the drag forces exerted by vegetation, and the associated wave dissipation, using frictionless linear wave theory to estimate the wave-induced water flows (hereafter 'wave orbital velocities') past plant stems. This approach provides a good approximation in sufficiently sparse canopies, but frictionless wave theory is not applicable at very high canopy densities. For near-bed vegetation, Lowe et al. (2005) (hereafter LKM05) derived a general and practical model for dissipation and vertically averaged wave orbital velocities applicable to very dense canopies. Extensions were developed for two-layer canopies (Weitzman et al., 2015) and random waves, and

* Corresponding author.

E-mail address: steve_henderson@wsu.edu (S.M. Henderson).

tested or calibrated against observed wave attenuation (Lowe et al., 2007; Jadhav et al., 2013). Zeller et al. (2015) found that major model simplifications can be justified in many natural canopies: often, acceleration-dependence of drag (resulting from Froude-Krylov forces and added mass, e.g. Sumer and Fredsøe (1997)) and vertical turbulent mixing can both be neglected at wave frequencies. Building on the approach of Zeller et al. (2015), we examine the properties of a simple model for wave orbital velocities, and test the model against observations within natural near-bed canopies of mangrove pneumatophores.

Previous laboratory experiments have quantified enhanced dissipation (Pujol et al., 2013a) and reduction of wave orbital velocities (Lowe et al., 2005; Luhar et al., 2010; Pujol et al., 2013b; Weitzman et al., 2015) by drag within artificial canopies. In natural canopies, many stems, each having its own unique size and shape, often create substantial vertical variability. Such vertical variability is quantified here using recently developed photogrammetric techniques, which measure the three-dimensional geometry of all stems within sampled regions of canopy (Liénard et al., 2016). Combining data from photogrammetric surveys with wave orbital velocities measured within natural pneumatophore canopies, we test a simple vertically resolved model derived from the equations of Zeller et al. (2015). The model is then applied to analyze the ability of Mekong Delta pneumatophore canopies to shelter onshore regions from incoming waves.

The model is outlined in Section 2, in turn considering within-canopy velocity (Section 2.1) and dissipation (Section 2.2). The field site, instrumentation, and data analysis are outlined in Section 3. Results are presented in Section 4, and summarized in Section 5.

2. Theory

2.1. Vertical variability of velocity induced by canopy drag

The vegetation canopy is described by statistics n = number of stems per square meter, d = mean stem diameter, a = cross-sectional area of vegetation blocking the flow per cubic meter of canopy (units m^{-1}), and ϕ = proportion of volume occupied by solid stems. For roughly cylindrical vertical stems, $a \approx nd$ and $\phi \approx (\pi/4)nd^2$. Here, n is a function of elevation z above the bed, because the number of stems usually decreases from a maximum at the bed to zero immediately above the elevation h_v of the highest stem (a , d and ϕ also vary with elevation).

As noted by Zeller et al. (2015), for many natural canopies $\phi \ll 1$, and at wave frequencies vertical mixing of momentum and acceleration-dependence of canopy drag forces are negligible (assumptions required for these simplifications are noted below and in Appendix A). For weakly nonlinear waves ($ul \ll c$, where c = wave phase speed), the horizontal momentum equation (e.g. eq.1.1 of Zeller et al. (2015), with turbulent and wave-induced momentum fluxes neglected) then reduces to

$$\frac{\partial u}{\partial t} + F_D + \frac{1}{\rho} \frac{\partial p}{\partial x} = 0, \quad (1)$$

where t = time, u = water velocity in horizontal direction x , ρ = water density, p = pressure, the canopy drag force per kilogram of water is

$$F_D = \frac{C_D}{2} aluu, \quad (2)$$

C_D is the drag coefficient for flow past a stem (here $C_D \approx 2$, Section 4), and lu is the magnitude of u . Therefore, acceleration [first term of (1)] results from vegetation drag (second term), and lateral pressure gradients (third term). Eq. (1) is obtained by averaging over a horizontal region encompassing many stems (Zeller et al., 2015), but extending substantially less than one wavelength in any direction. For a velocity u_b above the canopy, (1) reduces to

$$\frac{\partial u_b}{\partial t} + \frac{1}{\rho} \frac{\partial p}{\partial x} = 0. \quad (3)$$

Let

$$T_f = \frac{2}{C_D alul}. \quad (4)$$

Substituting $F_D = u/T_f$ [which follows from (2) and (4)] into (1) shows that T_f is a frictional timescale; if pressure forcing were negligible then drag would cause an initial velocity to decay over time of order T_f . Horizontal pressure gradients are initially assumed to be vertically uniform across the full height of the canopy, an assumption that will be relaxed at the end of this section. Pressure is eliminated by subtracting (3) from (1), leading to

$$\frac{\partial(u - u_b)}{\partial t} + \frac{u}{T_f} = 0. \quad (5)$$

From (5),

$$\frac{\text{Typical magnitude of } (u - u_b)}{\text{Typical magnitude of } u} = O(\Lambda_f), \quad (6)$$

where the ordering parameter

$$\Lambda_f = \frac{T_w}{2\pi T_f} = \frac{C_D alul T_w}{4\pi}, \quad (7)$$

T_w = typical wave period, and $O(\Lambda_f)$ denotes a term of order Λ_f . Strictly, the T_f defined by (4) varies over time, as lu varies. However, when evaluating ordering parameters such as Λ_f , we will simply use a typical time-constant value of T_f (the precise choice of this constant value will be clarified below). From (7), if the typical frictional timescale T_f is much longer than the wave period T_w then drag is insufficient to generate a large difference between within- and above-canopy velocities. From (6), nearbed canopies do little to shelter the bed from above-canopy wave motions if $\Lambda_f \ll 1$. Another interpretation for Λ_f is obtained by noting that the orbital displacement (i.e. the distance water particles move back and forth under waves) is of order lu/T_w . Furthermore, for randomly spaced stems, the average distance a water particle could travel in a straight horizontal line before encountering a stem is a^{-1} . Therefore, Λ_f is roughly the orbital displacement normalized by the typical distance particles travel before encountering stems.

The above discussion neglects vertical mixing. To make explicit the assumptions required for this simplification, we define

$$\epsilon_v = \frac{C_f lul T_w}{2\pi h_v}. \quad (8)$$

Scaling analysis (Appendix A) resembling the scaling of Zeller et al. (2015) establishes (1) from more general equations [e.g. from Eq. (4) of LKM05] given $u \ll c$, $\phi \ll 1$ and $\epsilon_v \ll \max\{\Lambda_f^{-1}, 1\}$. Under these conditions vertical mixing [neglected in (1) and (5)] is negligible through most of the canopy, although mixing remains significant in a thin neighborhood of the bed called the Wave Bottom Boundary Layer (WBBL, Mei, 1989).

For simplicity, we solve (5) for a time series discretely sampled at times $t_j = j\Delta t$, with j between $-N$ and N . Velocities are represented by the Fourier series

$$u = \sum_{j=-N}^N \langle u \rangle_{T_j} e^{i2\pi t/T_j}, \quad (9)$$

$$u_b = \sum_{j=-N}^N \langle u_b \rangle_{T_j} e^{i2\pi t/T_j}, \quad (10)$$

where, for any variable β , $\langle \beta \rangle_{T_j}$ denotes the complex amplitude at period $T_j = (2N + 1)\Delta t/j$. To derive a frequency-dependent model, we set lu to the constant value $(8/\pi)^{1/2} u_{rms}$ in (4), where u_{rms} is the root-mean-squared value of u . Here the factor $(8/\pi)^{1/2}$ was chosen to give the

correct mean value for dissipation, assuming a Gaussian velocity distribution. Similar approximations have been used for WBBL models (Tolman, 1994), for spectral models of forces on cylinders (Borgman, 1967), for simulating forces on saltmarsh vegetation (Mullarney and Henderson, 2010) and for simulating wave dissipation in coral and vegetation canopies (Lowe et al., 2007; Jadhav et al., 2013). From (5), (9), and (10), within- and above-canopy velocities are related by

$$\langle u \rangle_{T_j} = \tilde{\Gamma}_j \langle u_b \rangle_{T_j}, \quad (11)$$

where the transfer function

$$\tilde{\Gamma}_j = \frac{1}{1 - i\Lambda_{f,j}}, \quad (12)$$

and the value of $\Lambda_{f,j}$ for the j^{th} Fourier component is [c.f. (7)]

$$\Lambda_{f,j} = \frac{T_j}{2\pi T_f} = \frac{C_D a l u_l T_j}{4\pi}. \quad (13)$$

For small $\Lambda_{f,j}$, (12) predicts a small $O(\Lambda_{f,j})$ phase lead (within-canopy velocity ahead of overlying velocity), and a smaller $O(\Lambda_{f,j}^2)$ reduction in velocity amplitude. From (13), $\Lambda_{f,j}$ is proportional to wave period T_j , so both phase lead and amplitude attenuation increase with increasing period.

The solution (12) attributes all amplitude attenuation to canopy drag. However, even in the absence of drag, wave velocities decline with increasing depth unless the wavelength greatly exceeds the depth (i.e. unless waves are in shallow water). Frictionless linear wave theory predicts a ratio $\zeta = \cosh(kz_l)/\cosh(kz_u)$ between velocities at lower and upper elevations z_l and z_u , where $k = 2\pi/\text{wavelength}$ is calculated from the dispersion relation $(2\pi/T_j)^2 = gk \tanh(kh)$, and $g = 9.80 \text{ ms}^{-2}$ (Lowe et al., 2007). For the canopies considered here, such frictionless within-canopy depth attenuation will prove insignificant ($\zeta \approx 1$) for wave frequencies below about 0.3 Hz. At higher frequencies, ζ will drop substantially below 1, but for these cases $\tilde{\Gamma}_j \approx 1$. Therefore, a transfer function accounting for both frictional and frictionless vertical attenuation is

$$\Gamma_j = \frac{\zeta}{1 - i\Lambda_{f,j}}. \quad (14)$$

This prediction will be compared with observations.

2.2. Simulated dissipation

Neglecting bottom friction and directional spread, the depth-integrated wave energy balance at period T_j is

$$\frac{\partial E_{T_j} c_{g,j}}{\partial x} = - \int_0^h \mathcal{E}_{T_j} dz, \quad (15)$$

where x is the wave propagation direction, E_{T_j} is the spectral density of depth-integrated wave energy at period T_j , $c_{g,j}$ is the associated group velocity, and \mathcal{E}_{T_j} is the spectral density of dissipation by vegetation drag (a function of elevation). Let $\Phi_{T_j}(X, Y)$ be the cross spectrum at period T_j between any two time series X and Y (so $\Phi_{T_j}(X, X)$ is a power spectrum). The dissipation of wave energy by vegetation drag is the mean of uF_D , so from (2) and (11) the spectral density of dissipation is [c.f. Eq. (27) of Lowe et al. (2007) and Eq. (7) of Jadhav et al. (2013)]

$$\mathcal{E}_{T_j} = \frac{C_D a l u}{2} \Gamma^2 \Phi_{T_j}(u_b, u_b), \quad (16)$$

where the velocity u_b immediately above the pneumatophores will be approximated by the velocity predicted at the bed by frictionless linear wave theory (as is appropriate for near-bed canopies). Expressions (13)–(14) for Γ depend on within-canopy lu , which itself depends on Γ . To obtain an explicit predictive model for wave attenuation, an approximation for Γ in terms of above-canopy velocity $|u_b|$ is now derived. Since Γ_j is a slowly changing function of T_j , assuming a narrow-banded spectrum with peak period T_w , the transfer function is

approximated by a single value Γ_0 applicable to the entire (narrow) range of energetic frequencies (this approach, adopted for the remainder of this section, resembles Lowe et al. (2007)). Substituting $|\Gamma_0| = |u|/|u_b|$ into (13) and (14) then yields

$$\Gamma_0 = \frac{1}{1 - i\Lambda_0 |\Gamma_0|}, \quad (17)$$

where the dimensionless damping parameter

$$\Lambda_0 = \frac{C_D a l u_b |T_w}{4\pi} \quad (18)$$

differs from Λ_f in that the above-canopy velocity u_b appears in (18) whereas the within-canopy velocity u appears in (7). For $\Lambda_0 = 0$ (17) yields $\Gamma_0 = 1$, and for $\Lambda_0 > 0$ some algebra yields

$$|\Gamma_0|^2 = \frac{(1 + 4\Lambda_0^2)^{1/2} - 1}{2\Lambda_0^2}. \quad (19)$$

The depth-average of $|\Gamma_0|$ was denoted α_w by LKM05. The model considered here does not correspond to any of the simple limits (canopy-independent, inertia-dominated, or unidirectional) considered by LKM05. Consistent with the general analysis of LKM05, the orbital displacement (denoted A_{rms}^∞ by LKM05 and proportional to $|u_b|T_w$ here) is the sole hydrodynamic variable controlling $|\Gamma_0|$. However, $|\Gamma_0|$ here depends on only Λ_0 , which differs by a factor of order $\phi^{1/2} C_D / (2\pi^{3/2})$ from the parameter A_{rms}^∞ / S considered by LKM05, where the spacing between stems $S \approx n^{-1/2}$.

From (16), (18) and (19).

$$\mathcal{E}_{T_j} = \chi \frac{2\pi \Phi_{T_j}(u_b, u_b)}{T_w}, \quad (20)$$

where the dimensionless dissipation

$$\chi = \frac{[(1 + 4\Lambda_0^2)^{1/2} - 1]^{3/2}}{2^{3/2} \Lambda_0^2}. \quad (21)$$

Now $4\pi\chi$ is the ratio between the dissipation in one wave period and the above-canopy kinetic energy (both expressed per kilogram of water). For sufficiently sparse canopies ($\Lambda_0 \ll 1$), $\chi \approx \Lambda_0$, and since Λ_0 is proportional to a (18), increasing vegetation density is associated with increasing dissipation (Fig. 1). Expression (20) with $\chi = \Lambda_0$ could alternatively have been derived by simply neglecting all within-canopy attenuation of velocity (as was done, for example, by Dalrymple et al. (1984)), so this limit is called the ‘unattenuated dissipation model’. As Λ_0 increases above about 0.4 (vertical dotted line, Fig. 1), dissipation departs from the unattenuated prediction, and χ reaches a maximum of 1/2 when $\Lambda_0 = 2^{1/2}$. Further increase in Λ_0 reduces χ [$\chi \approx \Lambda_0^{-1/2}$ for

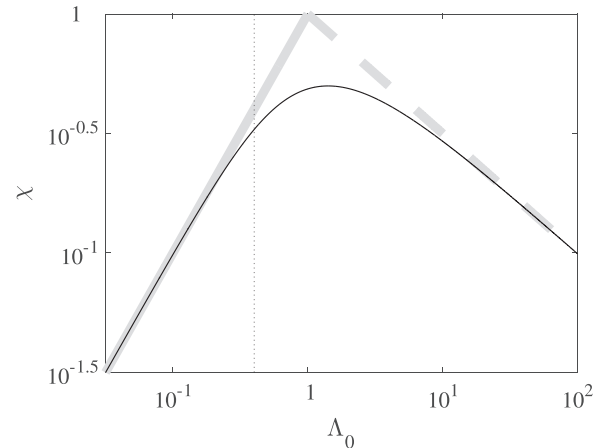


Fig. 1. Dimensionless dissipation χ [thin black curve, see Eqs. (20)–(21)] versus dimensionless damping parameter Λ_0 (18), showing maximum dissipation for order-one Λ_0 . Solid grey curve: approximation $\chi = \Lambda_0$, valid for $\Lambda_0 \ll 1$. Dashed grey curve: approximation $\chi = \Lambda_0^{-1/2}$, valid for $\Lambda_0 \gg 1$. Dotted black vertical line: $\Lambda_0 = 0.4$.

$\Lambda_0 \gg 1$]. Such complex behaviour is possible owing to reduced wave orbital velocities, and resulting reduced dissipation, within very dense canopies. Lowe et al. (2007) previously derived a more general model for this reduction in wave dissipation resulting from reduced within-canopy wave orbital velocities. The analysis here is novel in deriving an analytic expression, which highlights the importance of the damping parameter Λ_0 for the limit of low solid volume fraction ϕ and negligible vertical mixing.

Solution of the model (15), (18), (20), and (21) for waves propagating into a forest with variable geometry and bathymetry requires numerical integration. Nevertheless, the model could in principle be incorporated into a standard wave model such as SWAN (Appendix B). To simplify calculations below, we note that for $\Lambda_0 \ll 1$ and constant depth, the unattenuated model yields a simple analytic solution. From (18), (20), and $\chi \approx \Lambda_0$, the depth-integrated dissipation

$$\int_0^h \varepsilon_{T_j} dz = \frac{C_D \lambda |u_b|}{2} \Phi_{T_j}(u_b, u_b), \quad (22)$$

where

$$\lambda = \int_0^h a dz. \quad (23)$$

Substituting (22) and the linear wave theory result.

$E_{T_j} = (h/2)[1 + \sinh(2kh)/(2kh)]\Phi_{T_j}(u_b, u_b)$ into (15) and solving yields

$$E_{T_j} = \frac{E_0}{(1 + x/x_0)^2}, \quad (24)$$

where the dissipation length scale

$$x_0 = \frac{2hc_{g,j}[1 + \sinh(2kh)/(2kh)]}{C_D \lambda |u_0|} \quad (25)$$

is the distance waves propagate into the marsh before their amplitude is halved by dissipation, E_0 is the energy at $x = 0$, and $|u_0|$ is $|u_b|$ at $x = 0$. This closely resembles a solution found by Dalrymple et al. (1984), here simplified for a near-bed canopy.

3. Field site, instrumentation, and data analysis

Measurements were collected as part of the multi-investigator Mekong Tropical Delta Study (Ogston et al., 2017). We present measurements of water velocity and vegetation geometry obtained along the forested, ocean-exposed coast of Cù Lao Dung Island in the southern Mekong Delta (Fig. 2). Dense canopies of pneumatophore stems grow upward from the buried lateral roots of the dominant *Sonneratia caseolaris* mangroves. Two control deployments C1 and C2 were conducted on the unvegetated tidal flats, offshore of the forest edge. The remaining deployments P1–P5 sampled several locations within the forest, and several elevations within the pneumatophore canopy (Table 1). Deployments C1–C2 and P2–P4 were conducted within 15 m of forest-edge location N 9°29.5090', E 106°14.6377', near the southwest corner of Cù Lao Dung Island. Deployments P1 and P5 were conducted at the forest-edge location N 9°33.9296', E 106°17.5562', near the northeast corner of the Island. The pneumatophore canopies near the forest edge, sampled during P1–P5, were usually denser (larger n and d) than canopies farther into the forest interior. Additional deployment details are given by Norris et al. (2017); Mullarney et al. (2017).

During each deployment, a pair of vertically displaced current meters simultaneously measured velocities at 'lower' ($0.019 \text{ m} \leq z_l \leq 0.38 \text{ m}$) and 'upper' ($0.3 \text{ m} \leq z_u \leq 0.93 \text{ m}$) elevations (Columns 1–4, Table 1). During P1–P5, the lower and upper instruments respectively measured velocity within and above the pneumatophore canopy. Deployment numbers indicate the relative canopy density at the lower instrument elevation, with the lowest density for P1 and the highest density for P5. Instruments deployed in the low density case P2 are shown in Fig. 3a. 'Deployments' P1 and P5 actually refer to a single

case, with a vertical stack of three instruments (one above the canopy and two within the canopy). The upper and middle instruments were compared in 'Deployment P1', whereas the upper and lower instruments were compared in 'Deployment P5'. For P1 and P5, instruments were deployed for 20 h, and two different time series were used to obtain maximum sampling duration (one 4.8-h time series was centered on the first high tide observed during this deployment, and the second 4.5-h time series was centered on the second high tide; spectra from these two time series were averaged to yield the results presented, although similar results are obtained if these time series are analyzed separately). For remaining cases (C1–C2, P2–P4), measurement commenced soon after the upper instrument was submerged by the rising tide, and instruments were removed within a few hours, limiting sampling durations to < 158 min. Except for a few brief stoppages required for technical reasons, these time series were continuous. Deployments P3 and P4 were conducted at the same horizontal location on successive days, whereas each of C1, C2, and P2 was conducted at a different location. The lower instrument was always a Nortek Vectrino profiler, whereas the upper instrument was either a Vectrino profiler (deployments C1, P1, P5) or a Nortek Vector (C2, P2, P3, P4). Vectrino profilers measured velocity at 50 Hz every millimeter along a 35-mm profile. For deployments C1, P1, and P3, data from either end of each Vectrino profile were discarded, and velocities from the central 15 mm were averaged to yield a single 50-Hz time series for each Vectrino. For deployments C2, P2, P4, and P5, where the mid profile for the near-bed Vectrino was sometimes within 2 cm of the bed, velocities from the highest 5 mm of the profile were averaged, to minimize the influence of the WBBL (in these cases Vectrinos provided acoustic tracking of the bed, from which the mean sampling elevation z_l was determined). Vectors measured point velocity at 32 Hz, which was linearly interpolated to 50 Hz for comparison with Vectrino data. All Vectrinos were cabled to a single computer, whereas Vectors logged data internally. To synchronize Vectors with Vectrinos, Vector clock times were adjusted (usually by < 1 s) to ensure minimal phase shift between vertically displaced instruments at high (> 0.5 Hz) frequencies (these clock adjustments had minimal effect on phases at longer periods). Small ($< 5^\circ$) errors in rotation about the vertical axis were removed by optimizing the correlation between upper and lower velocity time series. Results are presented for horizontal velocity u in the mean wave direction (roughly onshore, and defined as the principal axis of measured 0.1–0.8 Hz velocity; Kuik et al. (1988)). Low ($< 70\%$) correlation data and spikes were replaced by linear interpolation.

Photographic surveys of pneumatophore canopies were conducted at low tide, within one day of corresponding current-meter deployments. Photographs obtained from many (55–387) angles around 1 m² quadrats centered on the current meters were used to reconstruct a three-dimensional point cloud using the open-source photogrammetric software VisualSFM (Fig. 3b). The diameter and location of every pneumatophore within each quadrat was estimated every 5 mm along vertical profiles extending from about $z = 0.03$ m to the top of the canopy, using the point cloud and the techniques developed by Liénard et al. (2016). For each of deployments P1–P5, vertical profiles of vegetation statistics n , d , a and ϕ were calculated from these data.

To test (14), empirical transfer functions between the upper velocity u_u and the lower velocity u_l were estimated. The variance of upper and lower velocities is quantified as a function of wave period by the power spectra $\Phi_{T_j}(u_u, u_u)$ and $\Phi_{T_j}(u_l, u_l)$. The cross-spectral matrix at period T_j between the upper and lower velocities is

$$M(T_j) = \begin{bmatrix} \Phi_{T_j}(u_u, u_u) & \Phi_{T_j}(u_u, u_l) \\ \Phi_{T_j}(u_l, u_u) & \Phi_{T_j}(u_l, u_l) \end{bmatrix}. \quad (26)$$

The (complex) dominant eigenvector of $M(T_j)$, denoted $(\tilde{u}_u, \tilde{u}_l)$, is the dominant EOF for period- T_j fluctuations in the two velocities (Henderson et al., 2001). An empirical transfer function was estimated from this dominant EOF as

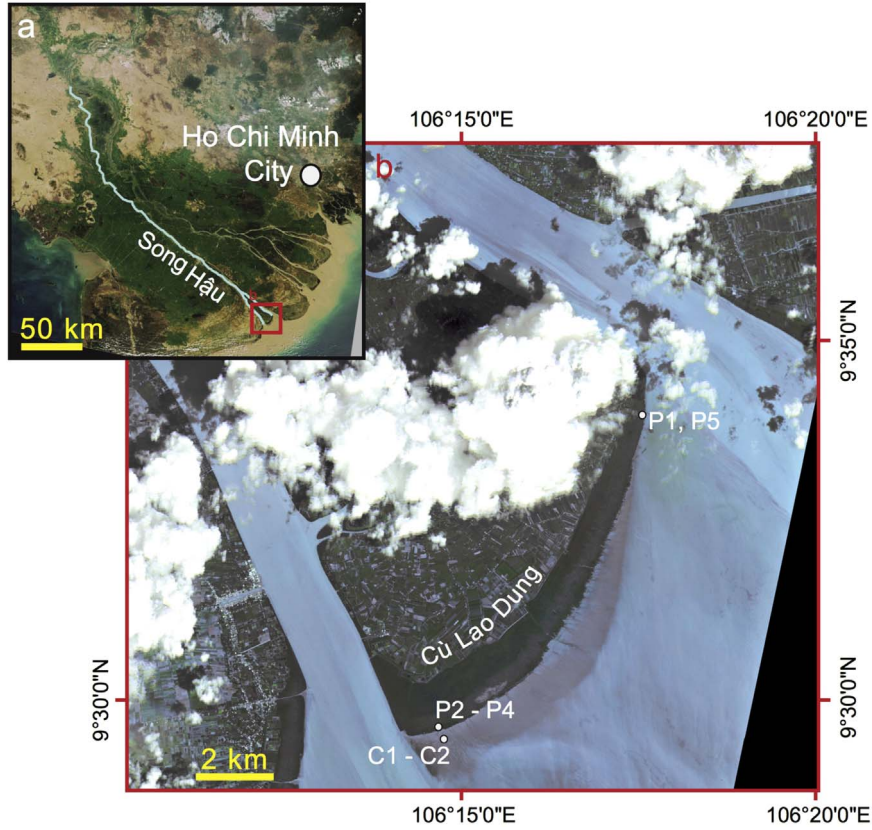


Fig. 2. Deployment Location. Top left (a): Broad view of deployment region (red square) within Mekong Delta. Lower right (b): detailed view, showing locations of pneumatophore (P1–P5) and control (C1, C2) deployments on seaward coast of Cù Lao Dung Island. In (b), blue regions correspond to open water (high tide), and dark green corresponds to forest. (For interpretation of the references to color in this figure legend, the reader is referred to the web version of this article.)

Table 1

Summary of deployments. z_l, z_u = elevations of lower and upper velocity measurements; vegetation area a evaluated at elevation z_l ; T_p = peak period of upper velocity spectrum; u_u = root-mean-square upper velocity magnitude; α = fitting parameter (theoretical value $C_D a$); Λ_0 = dimensionless damping parameter.

Label	Date	Duration (minutes)	z_l, z_u (m)	a (m^{-1})	T_p (s)	u_u (ms^{-1})	α	Λ_0
C1	9/27/2014	43	0.10, 0.30	0	2.0	0.29	0.012	0
C2	3/11/2015	45	0.019, 0.45	0	6.7	0.53	0.10	0
P1	3/13/2015	553	0.38, 0.81	0.14	2.2	0.28	0.16	0.015
P2	3/11/2015	37	0.028, 0.60	0.57	6.7	0.22	0.42	0.13
P3	3/8/2015	157	0.19, 0.93	0.58	5.9	0.20	1.0	0.17
P4	3/7/2015	129	0.021, 0.4	1.45	2.7	0.17	2.8	0.18
P5	3/13/2015	553	0.021, 0.81	1.78	2.2	0.28	4.2	0.38

$$\hat{r}_{T_j} = \frac{\hat{u}_l}{\hat{u}_u} \quad (27)$$

The magnitude and argument of this complex transfer function are respectively called the ‘Gain’ and the ‘Phase’ [the phase simply equals the phase of the cross spectrum $\Phi_{T_j}(u_u, u_l)$]. Since the estimated transfer function is meaningful only when upper and lower layers are coherent, we also present the squared coherence $|\Phi_{T_j}(u_u, u_l)|^2 / [\Phi_{T_j}(u_u, u_u)\Phi_{T_j}(u_l, u_l)]$. For each deployment, spectra were estimated using 50%-overlapping, hanning-windowed time-series segments (Welch, 1967), yielding > 50 degrees of freedom.

To compare theoretical and empirical transfer functions [(14) and

(27)], we write $\Lambda_{f,j} = \alpha |u| T_j / (4\pi)$, and for each deployment choose the single α value that minimizes the squared error $|G_{T_j} - \hat{r}_{T_j}|^2$ summed over all coherent frequencies (coherence² > 0.5). Here $|u|$ is calculated as $(8/\pi)^{1/2} u_{rms}$, where u_{rms} = root-mean-squared lower velocity. From (4) and (13), $\alpha = C_D a$, so a plot of α values obtained from multiple deployments against corresponding a values should show a positive correlation, with zero offset and slope equal to C_D . Laboratory experiments with oscillating cylinders indicate that C_D depends on the stem Reynolds number $Re_s = 2u_{rms}d/\nu_m$ and the Keulegan-Carpenter number $K_C = 2u_{rms}T_w/d$, where ν_m = kinematic viscosity of water and T_w is a peak period. For $Re = O(10^3)$ and $K_C = 50-300$, experiments suggest $C_D = 1-3$ (e.g. Sumer and Fredsøe, 1997).

To examine whether drag-induced reduction of within-canopy wave orbital velocities substantially reduced dissipation, Λ_0 was calculated from (18) and observations. The percentage overestimation in dissipation that would result from using the unattenuated model is $(\Lambda_0/\chi - 1) \times 100\%$.

4. Results

During the seven deployments, a ranged from 0 to 1.78 m^{-1} , peak wave periods ranged from 2.0 to 6.7 s, and rms velocity magnitudes ranged from 0.17 to 0.53 ms^{-1} (Table 1). During P1–P5, stem Reynolds numbers ranged from 3.3×10^3 to 5.4×10^3 , and Keulegan-Carpenter numbers ranged from 91 to 290.

Pneumatophore canopies were about 0.6 m high, with 45–84 stems m^{-2} , frontal area $a \leq 1.8 m^{-1}$, mean stem diameters $d \leq 0.028 m$, and solid volume fraction $\phi \leq 0.030$ (Fig. 4). The lowest density canopy was measured at the location of deployment P2 (light grey curves, Fig. 4, and pictured in Fig. 3). Although profiles of stem number and diameter differed between the location of deployments P1 and P5 and the location of deployments P3 and P4, the two locations showed

similar profiles of a (solid black and dashed dark grey curves, Fig. 4). In all cases, ϕ was sufficiently low that wake interference between stems (Tanino and Nepf, 2008) and acceleration-dependent forces were negligible.

During deployment C1, short-period, moderate-energy waves were observed (Table 1). As in all deployments, the velocity power spectrum was dominated by 0.1–1 Hz (hereafter ‘incident frequency’) waves (Fig. 5a). Upper and lower velocities were nearly equal at most incident frequencies, with similar power spectra (Fig. 5a), strong coherence (Fig. 5b), gain usually near 1 (Fig. 5c) and phase near zero (Fig. 5d). However, at the highest frequencies (> 0.5 Hz) the gain dropped, consistent with the depth attenuation predicted by frictionless linear wave theory (black dots and black dashed curve, Fig. 5c). At low frequencies (< 0.1 Hz), energy levels were low (Fig. 5a) and upper and lower velocities were only weakly coherent (Fig. 5b). Since surface wave velocities are essentially depth-uniform at these frequencies, these vertically incoherent low frequency motions were likely not surface waves, but may have been turbulent eddies. Fitting the model (14) to the observed transfer function (27) yields a transfer function near 1 (grey curves, Fig. 5c,d) and a fitting parameter α near zero (eighth column, Table 1), as expected in the absence of vegetation.

More energetic, longer period waves were observed during C2 (Table 1). As in deployment C1, upper and lower velocities were nearly

equal at 0.1–0.5 Hz, with some depth attenuation resembling the linear theory prediction at higher frequencies (Fig. 6a–d). At lower frequencies (< 0.1 Hz) a small phase shift was observed, with the lower velocity leading by about 5°. Gain also dropped below 1 at about 0.03 Hz. A gain < 1 and a phase lead up to 25° are expected within the WBL, and the lower current meter was near the bed ($z_l = 0.019$). Although the incident-frequency WBL was likely too thin to be measured by the lower current meter, boundary layer thickness increases with wave period (Mei, 1989), so the gain and phase observed at frequencies < 0.01 Hz may indicate the outer edge of the infragravity wave bottom boundary layer. Fitting the theoretical transfer function yields Γ near 1, and a fitting parameter α that is small, although not as small as in case C1 (Table 1). Regardless of the small phase shift at low frequencies, both C1 and C2 indicate that, in the absence of vegetation, depth-dependence at energetic incident frequencies was minimal, except for frictionless depth attenuation at the highest frequencies.

In contrast to deployments C1–C2 on the flats, clearer depth-dependence was observed within pneumatophores. Deployment P2, in a relatively low density canopy (Table 1), showed a phase shift of about 10° and 0.1 Hz (Fig. 7d). Consistent with theory, phase decreased with increasing frequency. The model (14) provides a reasonable fit to observations (compare black dots and grey curves, Fig. 7c,d), with a significantly non-zero fitting parameter α (Table 1). Nevertheless,

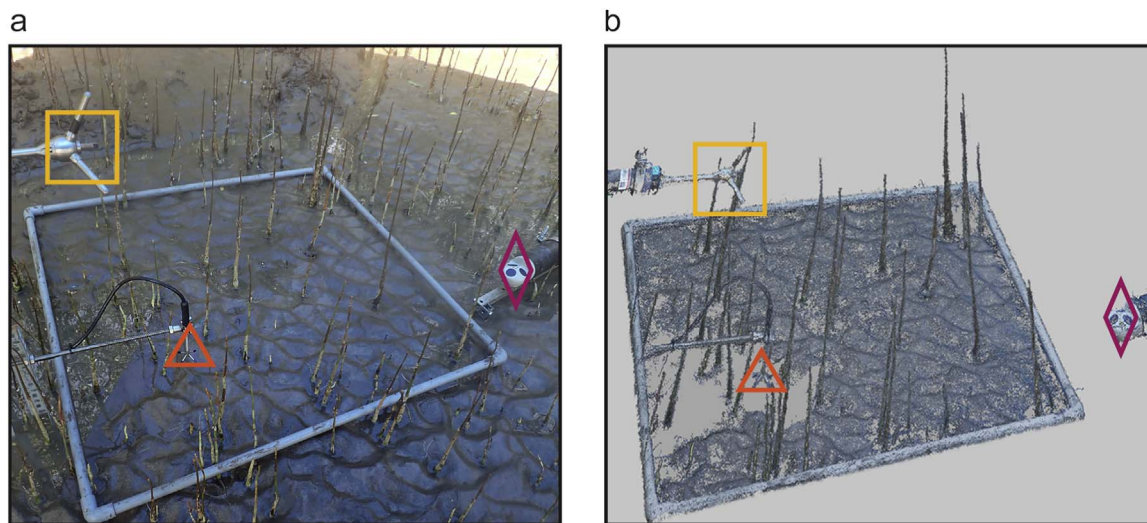


Fig. 3. Image (a) and three-dimensional reconstruction (b) of low-density pneumatophore canopy P2. The grey quadrat, marking one square meter, was removed before the incoming tide flooded the sampling region. The Vector (yellow square) and Vectrino (orange triangle) current meters measured above- and within-canopy velocity. The aquadopp current meter (red diamond) was not used here. (For interpretation of the references to color in this figure legend, the reader is referred to the web version of this article.)

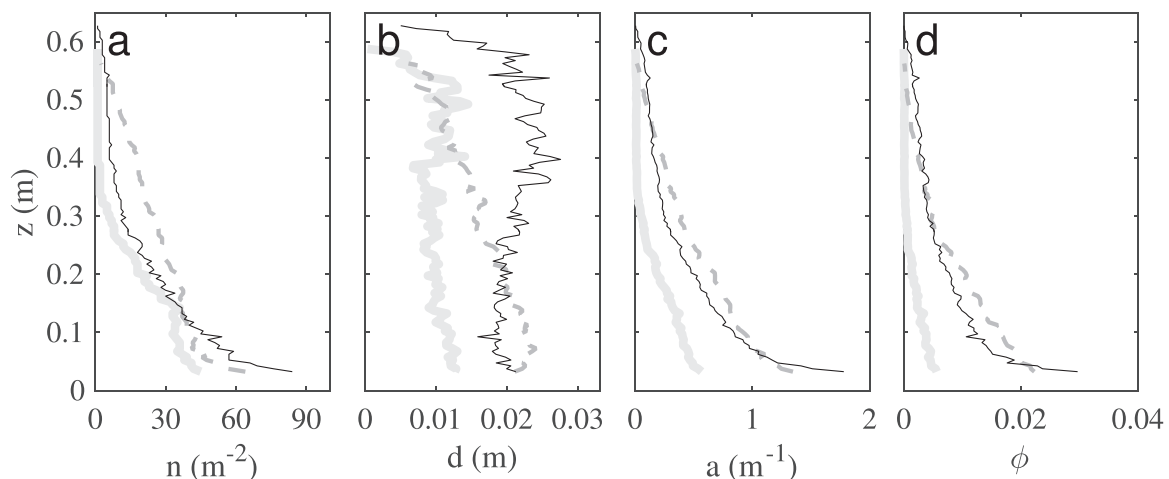


Fig. 4. Vertical profiles of vegetation statistics. (a): number of stems per square meter n . (b): mean stem diameter d . (c): frontal area a . (d): solid volume fraction ϕ . Thin black curves: canopy measured at location of deployments P1 and P5. Thick light grey: location of P2. Dashed dark grey: location of P3 and P4.

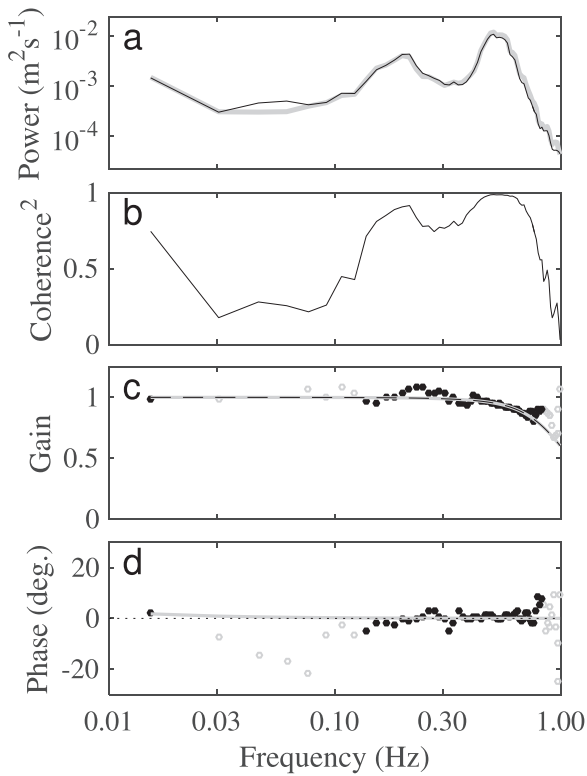


Fig. 5. Comparison of upper (elevation $z = 0.30$ m) and lower ($z = 0.10$ m) velocities measured over unvegetated tidal flats, Deployment C1, 27 September 2014. (a) power spectra of upper (grey) and lower (black) velocities. (b–d): Squared coherence (b), gain (c, < 1 indicates lower velocity smaller magnitude), and phase (c, positive indicates lower velocity leading) between upper and lower velocities. In (c)–(d), black (grey) dots indicate frequencies with squared coherence greater (less) than 0.5, and grey curves indicate fitted theoretical transfer function (14). In (c), black dashed curve, in this case indistinguishable from grey curve, indicates theoretical depth attenuation predicted by non-dissipative linear wave theory.

departures of the transfer function from the frictionless value ζ were small and the damping parameter $\Lambda_0 = 0.13$ was substantially less than 1. Results were similar for deployment P3 (Fig. 8), with clearer frictionless depth attenuation at high frequencies resulting from a relatively large separation of z_u and z_l . The greatest attenuation and phase shifts were observed in the high-density canopy of P5 (Fig. 9, note the extended vertical axis range of Fig. 9d). At low frequencies (< 0.03 Hz), gain approached zero and phase approached 90° (Fig. 9c,d), consistent with the $\Lambda_{f,j} \rightarrow \infty$ limit of (14), although associated coherence was low (Fig. 9b). The estimated $\Lambda_0 = 0.38$ was the largest for any deployment. Therefore, observations spanned the region to the left of the vertical black dotted line in Fig. 1, where the unattenuated model provides a good approximation (solid grey and black curves match). For $\Lambda_0 = 0.38$, the unattenuated model should overestimate dissipation by 20%.

As expected given the theoretical relationship $\alpha = C_D a$, values of α obtained by fitting transfer functions for the seven deployments were correlated with corresponding a values (Fig. 10). The best-fit slope suggests $C_D = 2.1$, comparable to values for oscillating cylinders at these Reynolds and Keulegan–Carpenter numbers. As expected given dominance by canopy drag (rather than the vertical mixing responsible for WBBL vertical structure), there is no tendency for velocities measured within 3 cm of the bed (black symbols, Fig. 10) to yield different α values than velocities measured at higher elevations (grey symbols).

For the observed small values of Λ_0 , the unattenuated model (25) provides an estimate of x_0 , i.e. the distance waves can propagate over uniform pneumatophore canopies before their amplitude is halved. Trapezoidal integration of measured a profiles yields λ (see (23)) of 0.095 (location of P2), 0.29 (location of P3, P4) and 0.28 (location of

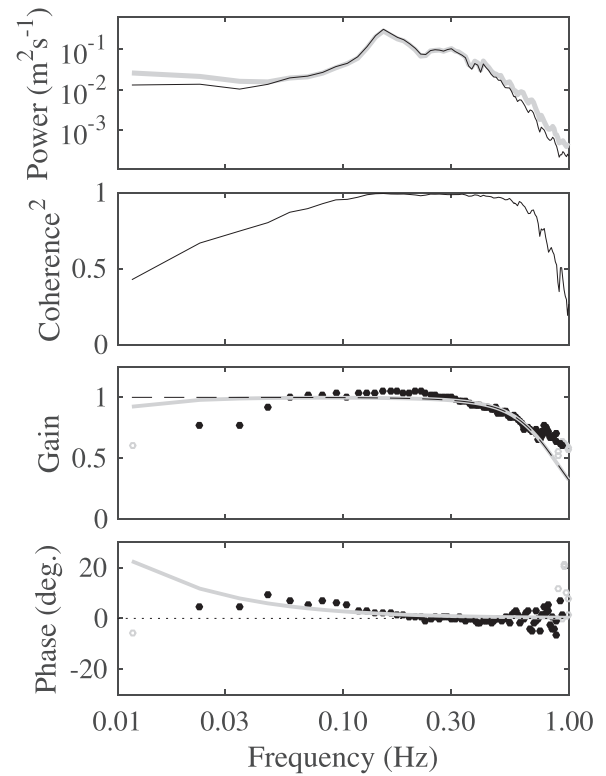


Fig. 6. As Fig. 5, but for deployment C2, over unvegetated tidal flats, 11 March 2015, upper and lower elevations $z = 0.45$ and 0.019 m.

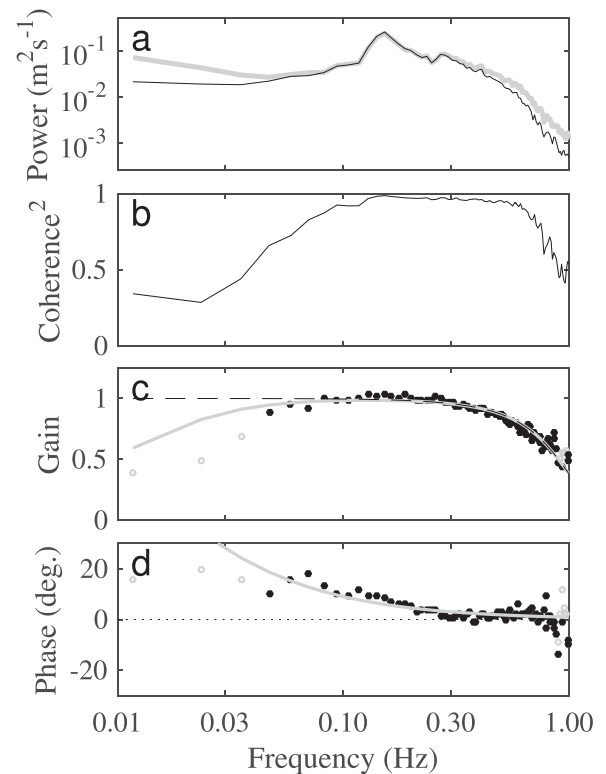


Fig. 7. As Fig. 5, but for deployment P2, vegetation density $a = 0.57$, 11 March 2015, upper and lower elevations $z = 0.60$ and 0.028 m.

P1, P5). Here, we focus on dissipation by pneumatophores, rather than tree trunks, because a values are much higher within pneumatophore canopies. Given $C_D = 2$, depth $h = 2$ m, and observed wave conditions, associated wave decay distances were 510 m (P2), 180 m (P3),

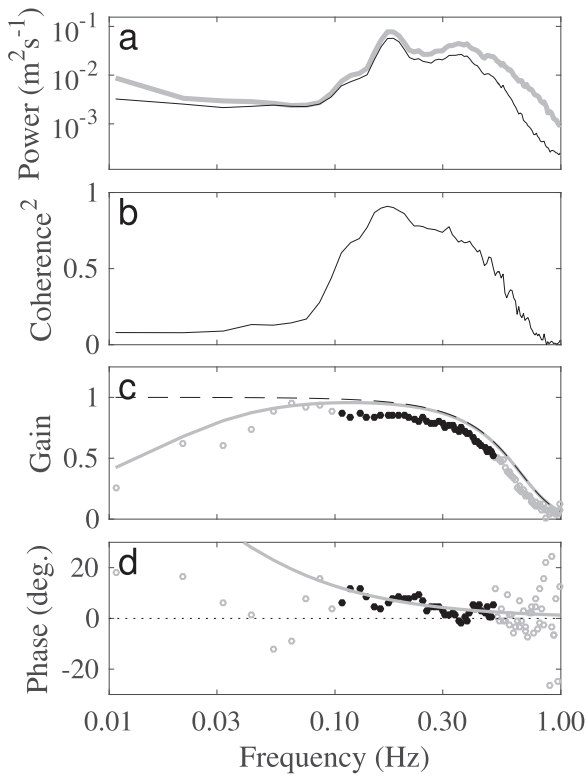


Fig. 8. As Fig. 5, but for deployment P3, vegetation density $a = 0.58$, 8 March 2015, upper and lower elevations $z = 0.93$ and 0.19 m.

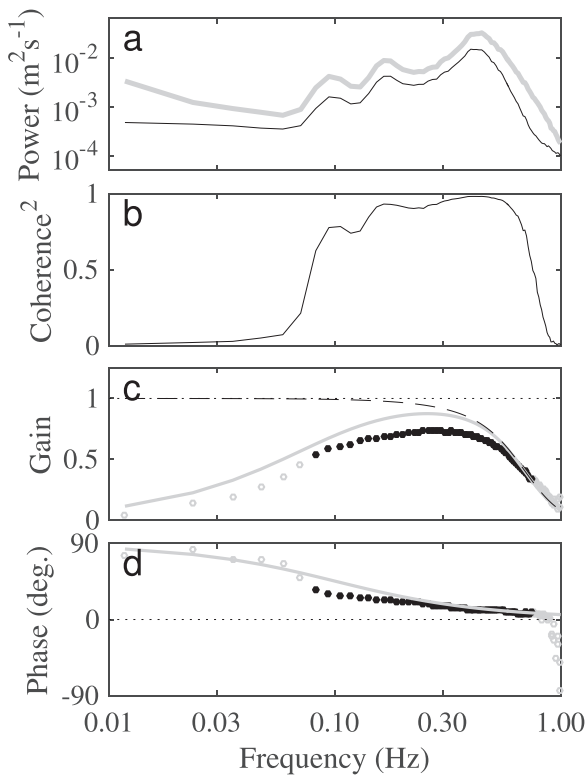


Fig. 9. As Fig. 5, but with extended y axis range, and for deployment P5, vegetation density $a = 1.78$, 13 March 2015, upper and lower elevations $z = 0.81$ and 0.021 m.

200 m (P4), and 180 m (P1, P5). Although these decay distances are large, predictions are sensitive to the assumed water depth; for a depth of 1 m, decay distances are reduced to 180 m (P2), 65 m (P3), 74 m (P4), and 48 m (P1, P5).

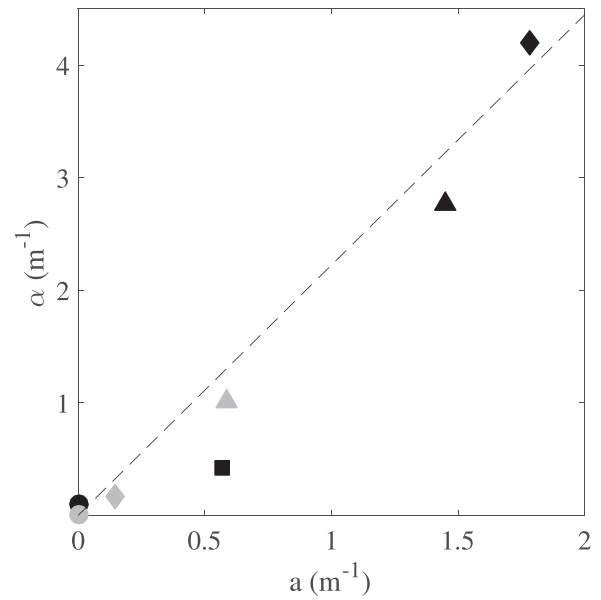


Fig. 10. Fitting parameter α for hydrodynamic model versus measured vegetation-density parameter a . Dashed line indicates theoretical relationship $\alpha = C_D a$ with best-fit $C_D = 2.1$. Deployment C1 grey circle, C2 black circle [partially obscured, near (0,0)], P1 grey diamond, P2 black square, P3 grey triangle, P4 black triangle, P5 black diamond. Black symbols: lower velocity measured at elevation $z_l < 0.03$ m above bed (grey symbols: $z_l > 0.03$ m).

5. Summary

On Cù Lao Dung Island in the Mekong Delta, wave orbital velocities measured within pneumatophore canopies were roughly consistent with a simple model (Zeller et al., 2015) that neglects vertical mixing and acceleration-dependent drag. Frequency dependence matched an analytic solution predicted using a linearized drag law. When solving for the dissipation of all wave energy (rather than frequency dependence) the model considered here is nonlinear, but sufficiently simple that an analytic solution relates within-canopy flow to above-canopy flow.

In low density canopies, within-canopy velocities are only slightly reduced by canopy drag and modeled dissipation is proportional to canopy density, measured by a . Conversely, in sufficiently high density canopies, increasing density can reduce near-bed flows enough to reduce dissipation (dissipation proportional to $a^{-1/2}$). The transition between the low- and high-density regimes is controlled by a dimensionless parameter Λ_0 (18), which is a function of both canopy geometry and hydrodynamic conditions; dissipation is maximum at the transition between low- and high-density regimes, which occurs near $\Lambda_0 = 1.4$ (Fig. 1). Therefore, the parameter Λ_0 plays a role in analysis of fluctuating flows resembling that of the parameter λ (Nepf, 2012) in analysis of steady flows: relative to above-canopy flows, fluctuating (or steady) flow is greatly reduced within a nearbed canopy if and only if Λ_0 (or λ) is sufficiently large. Despite this resemblance, the physical forcing differs between the fluctuating and steady cases, with the former forced by horizontal pressure gradients and the latter by shear stresses (Nepf, 2012).

The pneumatophore canopies and hydrodynamic conditions we measured on Cù Lao Dung Island were in the low-density regime ($\Lambda_0 \leq 0.38$). This finding is consistent with the increase in within-canopy turbulent dissipation with increasing a found by Norris et al. (2017). Nevertheless, Λ_0 was not much less than 1, so occasional departure from the low-density regime remains likely. For one observed case (P5), a doubling of wave period and wave height, plausible in storm conditions, would yield $\Lambda_0 = 1.5$, at the boundary between low- and high-density regimes. In this case, using frictionless linear theory to estimate within-canopy velocity would yield wave-dissipation estimates triple the true value. Elevated dissipation within

pneumatophores may enhance sediment mobilization (Norris et al., 2017), whereas sheltering of the bed at high canopy densities could create conditions for rapid deposition. Rapid deposition can bury pneumatophores, reducing mangrove vigor or even causing death (Nardin et al., 2016; Moffett et al., 2015; Ellison, 1999). Therefore, the tendency for observed pneumatophore canopies to approach, but seldom exceed, the density of maximum dissipation may be adaptive.

Theory suggests that the low-density ($\Lambda_0 \ll 1$) and transitional (Λ_0 order-one) regimes found for mangrove pneumatophores on Cù Lao Dung Island are common across a wide range of aquatic plant canopies, although occasional high-density ($\Lambda_0 \gg 1$) cases are also found. For example, $\Lambda_0 = 0.14\text{--}0.43$ for *Avicennia marina* mangrove pneumatophores measured in New Zealand ($n = 200\text{ m}^{-2}$, Young and Harvey (1996), $d = 7 \times 10^{-3}\text{ m}$, $u_{rms} = 0.1\text{--}0.3\text{ ms}^{-1}$, $T_w = 4\text{ s}$). Higher a values have been observed in the prop roots of the mangrove *Rhizophora stylosa* (Mazda et al., 1997). In temperate saltmarshes, observations of the sedge *Schenoplectus americanus* yield $\Lambda_0 = 0.17\text{--}0.50$ ($n = 650\text{ m}^{-2}$, $d = 5 \times 10^{-3}\text{ m}$, $u_{rms} = 0.1\text{--}0.3\text{ ms}^{-1}$, $T_w = 2\text{ s}$, Mullarney and Henderson (2010)), and observations of the marsh grass *Spartina alterniflora* yield $\Lambda_0 = 0.33\text{--}0.98$ ($n = 400\text{ m}^{-2}$, $d = 8 \times 10^{-3}\text{ m}$, $u_{rms} = 0.1\text{--}0.3\text{ ms}^{-1}$, $T_w = 4\text{ s}$, Jadhav et al. (2013)). Depending on hydrodynamic conditions, seagrasses such as *Thalassia testudinum* may sometimes approach the high-density regime (e.g. $\Lambda_0 = 3.4$ for $n = 1100\text{ m}^{-2}$, $d = 10^{-2}\text{ m}$, $u_{rms} = 0.3\text{ ms}^{-1}$, $T_w = 4\text{ s}$, Luhar and Nepf (2011); Bradley and Houser (2009)) and sometimes are in the low-density regime (e.g. $\Lambda_0 = 0.074$ for $u_{rms} = 0.02\text{ ms}^{-1}$, $T_w = 1.33\text{ s}$, as observed by Bradley and Houser (2009)). The theory developed here neglects stem motion, and can be applied to the flexible species noted above only near the bed, where stem motion is minimal (for analysis of flexible cases, see Mullarney and Henderson, 2010; Luhar and Nepf, 2016).

Appendix A. : Scaling

This section examines the magnitude of neglected momentum mixing, relative to the terms retained in (1). In the limit of small ϕ (denoted λ_p by LKM05), subtracting our Eq. (3) from Eq. (4) of LKM05 yields

$$\frac{\partial u_d}{\partial t} + \frac{u}{T_f} - \nu \frac{\partial^2 u_d}{\partial z^2} = 0, \quad (\text{A.1})$$

where the defect velocity $u_d = u - u_b$, the eddy viscosity $\nu = \tau_w / (\rho \partial u / \partial z)$, and τ_w is the turbulent shear stress. Dimensionless variables, denoted by $*$, are defined by

$$t = \frac{T_w T_*}{2\pi}, \quad (\text{A.2})$$

$$z = h_v z_*. \quad (\text{A.3})$$

Consider separately the cases $\Lambda_f \leq 1$ and $\Lambda_f > 1$.

A.1. Case $\Lambda_f \leq 1$

For moderate or weak attenuation of within-canopy velocity, define dimensionless variables by

$$u = u_0 u_*, \quad (\text{A.4})$$

$$u_d = \Lambda_f u_0 u_{d*}, \quad (\text{A.5})$$

$$\nu = \Lambda_f C_f u_0 h_v \nu_*, \quad (\text{A.6})$$

where u_0 is a typical amplitude of above-canopy velocity fluctuations, and $C_f \sim 0.1$ (c.f. Lowe et al., 2005; Weitzman et al., 2015). Scaling (A.5) is appropriate because, when canopy friction is very small (i.e. when $\Lambda_f \ll 1$), within-canopy velocity approaches above-canopy velocity and u_d becomes small (order Λ_f). A Prandtl mixing-length scaling $\nu = \ell^2 |\partial u / \partial z|$ (Monin and Yaglom, 1975) yields (A.6) given a mixing length $\ell \sim h_v$ and $\partial u / \partial z \sim u_d / h_v$. Now (A.1) becomes

$$\frac{\partial u_{d*}}{\partial t_*} + u_* - \Lambda_f \epsilon_\nu \nu_* \frac{\partial^2 u_{d*}}{\partial z_*^2} = 0, \quad (\text{A.7})$$

so mixing is negligible if $\Lambda_f \epsilon_\nu \ll 1$.

The above discussion suggests that the mangrove pneumatophore canopies observed in the Mekong Delta (like many other natural canopies) provide the bed little shelter from above-canopy wave motions, and may even enhance sediment suspension. Nevertheless, by enhancing dissipation at the forest edge, pneumatophores do reduce the height of waves propagating into the forest interior. Theory for low canopy density ($\Lambda_0 \ll 1$), resembling the model of Dalrymple et al. (1984), predicts strong depth-dependence to this sheltering effect, qualitatively consistent with previous observations (Mazda et al., 2006). For observed waves and pneumatophore canopies, simulations predict that waves dissipated substantially as they propagated tens of meters in 1 m water depth, or hundreds of meters in 2 m depth (propagation distances would be shorter under higher wave energies). However, the observations reported here were collected near the forest fringe, where canopies were relatively dense (Norris et al., 2017). Therefore, lower canopy densities might lead to reduced dissipation in the forest interior.

Acknowledgements

During fieldwork in Vietnam, vital logistical support was provided by Huong Phuoc Vu Luong, Charles Nittrouer, Richard Nguyen, Andrea Ogston, and Daniel Culling. Further assistance at the field site was provided by Dean Sandwell, Aaron Fricke, Daniel Culling, Sergio Fagherazzi, William Nardin, Xuan Tien Nguyen Vinh, and Hoang Phong Nguyen. Imagery for Fig. 2 was provided by MDA Information Systems LLC. We thank the editor and the reviewers for their suggestions. Fieldwork was funded by the US Office of Naval Research, Littoral Geosciences grant number N000141410112, and the Office of Naval Research Global grant number N62909-14-1-N028.

A.2. Case $\Lambda_f > 1$

When $\Lambda_f \gg 1$, (A.5) and (A.6) are inappropriate because u_d cannot become much larger than the above-canopy velocity u_b . Instead, for $\Lambda_f \gg 1$, within-canopy velocity u becomes small (order Λ_f^{-1}) and $u_d = u - u_b \approx -u_b$. Therefore we rescale

$$u_b = u_0 u_{b*}, \quad (\text{A.8})$$

$$u = \frac{u_0 u_*}{\Lambda_f}, \quad (\text{A.9})$$

$$u_d = u_0 u_{b*}, \quad (\text{A.10})$$

$$\nu = C_f u_0 h_\nu \nu_*. \quad (\text{A.11})$$

Neglecting terms of order Λ_f^{-1} , (A.1) becomes

$$-\frac{\partial u_{b*}}{\partial t_*} + u_* - \epsilon_\nu \nu_* \frac{\partial^2 u_{d*}}{\partial z_*^2} = 0, \quad (\text{A.12})$$

so mixing is negligible if $\epsilon_\nu \ll 1$.

For given ϵ_ν , comparison of (A.7) and (A.12) indicates that vertical mixing is less likely to be significant when $\Lambda_f \ll 1$. This is because the case of minimal canopy drag ($\Lambda_f \ll 1$) is associated with minimal shear ($u_d \ll u_0$), minimal shear production, and a small eddy viscosity.

A.3. Application to field case

Consider case P5, with $|u| = (8/\pi)^{1/2} \times 0.28 \text{ ms}^{-1}$, $T_w = 2.2 \text{ s}$, and $h_v = 0.6 \text{ m}$. Now $\epsilon_\nu = 0.026 \ll 1$, so momentum mixing was negligible. Next, consider case P2, for which $|u| = (8/\pi)^{1/2} \times 0.22 \text{ ms}^{-1}$, $T_w = 6.7 \text{ s}$, and $h_v = 0.6 \text{ m}$. Now $\epsilon_\nu = 0.062$, and since $\Lambda_0 = 0.13 \ll 1$, the relative importance of mixing scaled with $\Lambda_f \epsilon_\nu = 0.0081 \ll 1$. Similar calculations indicate that estimated momentum mixing was small in all cases considered.

Appendix B. : Potential for implementation in spectral wave models

In response to a reviewer's question, we sketch out an approach by which vegetation-induced wave dissipation could be added to other source terms in the action balance of spectral wave models such as SWAN (Booij et al., 1999). Dissipation, as modeled here, could be calculated within a subroutine, which would require as inputs the wave energy spectrum E_{T_j} calculated at a set of periods $\{T_j\}$, the water depth h , and $a(z_k)$ specified at a set of near-bed elevations $\{z_k\}$. Dissipation can then be calculated using the following steps:

1. The spectrum $\Phi_{T_j}(u_b, u_b)$ of near-bed velocity is calculated from E_{T_j} and h using linear theory (for directionally-spread waves, it may be simplest to replace $\Phi_{T_j}(u_b, u_b)$ with $\Phi_{T_j}(u_b, u_b) + \Phi_{T_j}(v_b, v_b)$, where v_b is the horizontal velocity perpendicular to u_b). The peak frequency T_w of this spectrum is calculated, the spectrum is integrated to calculate $u_{b,rms}$, and $|u_b|$ is set to $(8/\pi)^{1/2} u_{b,rms}$.
2. $\Lambda_0(z_k)$ is calculated from (18) along a vertical profile (i.e. for every z_k).
3. A vertical profile of $|V_0(z_k)|$ is calculated from (19).
4. A vertical profile of $|u(z_k)|$ is calculated from $|u(z_k)| = |V_0(z_k)| |u_b|$.
5. For every T_j , a vertical profile of $\Lambda_{f,j}$ is calculated from (13).
6. For every T_j , a vertical profile of $\Gamma_j(z_k)$ is calculated from (12) (here we neglect within-canopy depth-attenuation of pressure).
7. For every T_j , a vertical profile of dissipation $\mathcal{E}_{T_j}(z_k)$ is calculated using (16).
8. For every T_j , vertical integration of $\mathcal{E}_{T_j}(z_k)$ yields depth-integrated dissipation.

All steps require only evaluation of simple formulas, and the computational cost might be small if only a few vertical gridpoints z_k were used.

References

- Anthony, E.J., Brunier, G., Besset, M., Goichot, M., Dussouillez, P., Nguyen, V.L., 2015. Linking rapid erosion of the Mekong river delta to human activities. *Sci. Rep.*, 5. <http://dx.doi.org/10.1038/srep14745>.
- Bao, T., 2011. Effect of mangrove forest structures on wave attenuation in coastal Vietnam. *Oceanologia* 53 (3), 807–818. (<http://dx.doi.org/10.5697/oc.53-3.807>).
- Booij, N., Ris, R., Holthuijsen, L., 1999. A third-generation wave model for coastal regions 1. model description and validation. *J. Geophys. Res.* 104, 7649–7666. <http://dx.doi.org/10.1029/98JC02622>.
- Borgman, L., 1967. Spectral analysis of wave forces on piling. *J. Waterw. Harb. Div., ASCE* 93, 129–156.
- Bouma, T., van Duren, L., Temmerman, S., Claverie, T., Blanco-Garcia, A., Ysebaert, T., Herman, P., 2007. Spatial flow and sedimentation patterns within patches of epibenthic structures: combining field, flume and modelling experiments. *Cont. Shelf Res.* 27, 1020–1045. (<http://dx.doi.org/10.1016/j.csr.2005.12.019>).
- Bradley, K., Houser, C., 2009. Relative velocity of seagrass blades: implications for wave attenuation in low-energy environments. *J. Geophys. Res.*, 114. <http://dx.doi.org/10.1029/2007JF000951>.
- Dalrymple, R.A., Kirby, J., Hwang, P., 1984. Wave diffraction due to areas of energy dissipation. *J. Waterw., Port., Coast., Ocean Eng.* 110, 67–79. ([http://dx.doi.org/10.1061/\(ASCE\)0733-950X\(1984\)110:1\(67\)](http://dx.doi.org/10.1061/(ASCE)0733-950X(1984)110:1(67))).
- Ellison, J.C., 1999. Impacts of sediment burial on mangroves. *Mar. Pollut. Bull.* 37 (812), 420–426. ([http://dx.doi.org/10.1016/S0025-326X\(98\)00122-2](http://dx.doi.org/10.1016/S0025-326X(98)00122-2)).
- Furukawa, K., Wolanski, E., Mueller, H., 1997. Currents and sediment transport in mangrove forests. *Estuar., Coast. Shelf Sci.* 44, 301–310. (<http://dx.doi.org/10.1006/ecss.1996.0120>).
- Giri, C., Ochieng, E., Tieszen, L., Zhu, Z., Singh, A., Loveland, T., Masek, J., Duke, N., 2011. Status and distribution of mangrove forests of the world using earth observation satellite data. *Glob. Ecol. Biogeogr.* 20, 154–159. <http://dx.doi.org/10.1111/j.1466-8238.2010.00584.x>.
- Greenberg, R., Maldonado, J., Droege, S., McDonald, M., 2006. Tidal marshes: a global perspective on the evolution and conservation of their terrestrial vertebrates. *Bioscience* 56, 675–685. ([http://dx.doi.org/10.1641/0006-3568\(2006\)56\[675:TMAGPO\]2.0.CO;2](http://dx.doi.org/10.1641/0006-3568(2006)56[675:TMAGPO]2.0.CO;2)).
- Henderson, S.M., Elgar, S., Bowen, A., 2001. Observations of surf beat propagation and energetics. In: Proceedings of the 27th International Conference on Coastal Engineering, pp. 1412–1421. ([http://dx.doi.org/10.1061/40549\(276\)109](http://dx.doi.org/10.1061/40549(276)109)). ASCE.
- Horstman, E.M., Dohmen-Janssen, C.M., Narra, P.M.F., van den Berg, N.J.F., Siemerink, M., Hulscher, S.J.M.H., 2014. Wave attenuation in mangroves: A quantitative approach to field observations. *Coast. Eng.* 94, 47–62. (<http://dx.doi.org/10.1016/j.coastaleng.2014.08.005>).
- Jadhav, R.S., Chen, Q., Smith, J.M., 2013. Spectral distribution of wave energy dissipation by salt marsh vegetation. *Coast. Eng.* 77, 99–107. <http://dx.doi.org/10.1016/j.coastaleng.2013.02.013>.
- Kuik, A., Van Vledder, G.P., Holthuijsen, L., 1988. A method for routine analysis of pitch-and-roll buoy wave data. *Journal of Physical Oceanography*, 18:1020–1034. ([http://dx.doi.org/10.1175/1520-0485\(1988\)0181020:AMFTRA2.0.CO;2](http://dx.doi.org/10.1175/1520-0485(1988)0181020:AMFTRA2.0.CO;2)).
- Liénard, J., Lynn, K., Strigul, N., Norris, B., Gatzliolis, D., Mullarney, J.C., Bryan, Karin, R., Henderson, S.M., 2016. Efficient three-dimensional reconstruction of aquatic vegetation geometry: estimating morphological parameters influencing

- hydrodynamic drag. *Estuar., Coast., Shelf Sci.* 178, 77–85, (<http://dx.doi.org/10.1016/j.ecss.2016.05.011>).
- Lowe, R.J., Falter, J.L., Koseff, J.R., Monismith, S.G., Atkinson, M.J., 2007. Spectral wave flow attenuation within submerged canopies: implications for wave energy dissipation. *J. Geophys. Res.: Oceans* 112 (C5), C05018. <http://dx.doi.org/10.1029/2006JC003605>.
- Lowe, R.J., Koseff, J.R., Monismith, S.G., 2005. Oscillatory flow through submerged canopies: 1. velocity structure. *J. Geophys. Res.*, 110. <http://dx.doi.org/10.1029/2004JC002788>.
- Luhar, M., Coutu, S., Infantes, E., Fox, S., Nepf, H.M., 2010. Wave-induced velocities inside a model seagrass bed. *J. Geophys. Res.*, 115. <http://dx.doi.org/10.1029/2010JC006345>.
- Luhar, M., Nepf, H.M., 2011. Flow-induced reconfiguration of buoyant and flexible aquatic vegetation. *Limnol. Oceanogr.* 55, 2003–2017. <http://dx.doi.org/10.4319/lo.2011.56.6.2003>.
- Luhar, M., Nepf, H.M., 2016. Wave-induced dynamics of flexible blades. *J. Fluids Struct.* 61, 20–41, (<http://dx.doi.org/10.1016/j.jfluidstructs.2015.11.007>).
- Mazda, Y., Magi, M., Ikeda, Y., Kurokawa, T., Asano, T., 2006. Wave reduction in a mangrove forest dominated by *Sonneratia* sp. *Wetl. Ecol. Manag.* 14, 365–378. <http://dx.doi.org/10.1007/s11273-005-5388-0>.
- Mazda, Y., Wolanski, E., Kin, B., Sase, A., Ohtsuka, D., Magi, M., 1997. Drag force due to vegetation in mangrove swamps. *Mangroves Salt Marshes* 1, 193–199. <http://dx.doi.org/10.1023/A:1009949411068>.
- Mei, C.C., 1989. *The Applied Dynamics of Ocean Surface Waves*. World Scientific, New Jersey.
- Moffett, K.B., Nardin, W., Silvestri, S., Wang, C., Temmerman, S., 2015. Multiple stable states and catastrophic shifts in coastal wetlands: progress, challenges, and opportunities in validating theory using remote sensing and other methods. *Remote Sens.* 7, 10184–10226. <http://dx.doi.org/10.3390/rs70810184>.
- Monin, A., Yaglom, A., 1975. *Statistical Fluid Mechanics: Mechanics of Turbulence*. Dover, New York.
- Mullarney, J.C., Henderson, S.M., 2010. Wave-forced motion of submerged single stem vegetation. *J. Geophys. Res.*, 115. <http://dx.doi.org/10.1029/2010JC006448>.
- Mullarney, J.C., Henderson, S.M., Reynolds, J.A.H., Norris, B.K., Bryan, K.R., 2017. Spatially varying drag within a wave-exposed mangrove forest and on the adjacent tidal flat. *Continental Shelf Research*, 147, 102–113.
- Nardin, W., Woodcock, C.E., Fagherazzi, S., 2016. Bottom sediments affect *Sonneratia* mangrove forests in the prograding Mekong delta, Vietnam. *Estuar., Coast. Shelf Sci.* 177, 60–70, (<http://dx.doi.org/10.1016/j.ecss.2016.04.019>).
- Nepf, H.M., 2012. Flow and transport in regions with aquatic vegetation. *Annu. Rev. Fluid Mech.* 44, 123–142. <http://dx.doi.org/10.1146/annurev-fluid-120710-101048>.
- Nicholls, R., Hoozemans, F., Marchand, M., 1999. Increasing flood risk and wetland losses due to global sea-level rise: regional and global analyses. *Glob. Environ. Change - Human. Policy Dimens.* 9, S69–S87, ([http://dx.doi.org/10.1016/S0959-3780\(99\)00019-9](http://dx.doi.org/10.1016/S0959-3780(99)00019-9)).
- Norris, B.K., Mullarney, J.C., Bryan, K.R., Henderson, S.M., 2017. The effect of pneumatophore density on turbulence: A field study in a *Sonneratia*-dominated mangrove forest, Vietnam. *Continental Shelf Research*, 147, 114–127. <http://dx.doi.org/10.1016/j.csr.2017.06.002>.
- Ogston, A., Allison, M., Mullarney, J., Nittrouer, C., 2017. Sediment- and hydrodynamics of the mekong delta: from tidal river to continental shelf. *Continental Shelf Research*, 147, 1–6.
- Pujol, D., Casamitjana, X., Serra, T., Colomer, J., 2013a. Canopy-scale turbulence under oscillatory flow. *Cont. Shelf Res.* 66, 9–18, (<http://dx.doi.org/10.1016/j.csr.2013.06.012>).
- Pujol, D., Serra, T., Colomer, J., Casamitjana, X., 2013b. Flow structure in canopy models dominated by progressive waves. *J. Hydrol.* 486, 281–292, (<http://dx.doi.org/10.1016/j.jhydrol.2013.01.024>).
- Riffe, K.C., Henderson, S.M., Mullarney, J.C., 2011. Wave dissipation by flexible vegetation. *Geophys. Res. Lett.*, 38. <http://dx.doi.org/10.1029/2011GL048773>.
- Siikamäki, J., Sanchirico, J.N., Jardine, S.L., 2012. Global economic potential for reducing carbon dioxide emissions from mangrove loss. In: *Proceedings of the National Academy of Sciences of the United States of America*, 109(36): pp. 14369–14374. <http://dx.doi.org/10.1073/pnas.1200519109>.
- Sumer, B., Fredsoe, J., 1997. *Hydrodynamics Around Cylindrical Structures*. Advanced Series in Applied Physics. World Scientific.
- Tanino, Y., Nepf, H.M., 2008. Laboratory investigation of mean drag in a random array of rigid, emergent cylinders. *J. Hydraul. Eng.* 134 (1), 34–41. [http://dx.doi.org/10.1061/\(ASCE\)0733-9429\(2008\)134:1\(34\)](http://dx.doi.org/10.1061/(ASCE)0733-9429(2008)134:1(34)).
- Temmerman, S., Meire, P., Bouma, T., Herman, P., Ysebaert, T., De Vriend, H., 2013. Ecosystem-based coastal defence in the face of global change. *Nature* 504, 79–83. <http://dx.doi.org/10.1038/nature12859>.
- Thu, P.M., Populus, J., 2007. Status and changes of mangrove forest in Mekong Delta: case study in Tra Vinh, Vietnam. *Estuar., Coast. Shelf Sci.* 71 (1–2), 98–109. <http://dx.doi.org/10.1016/j.ecss.2006.08.007>.
- Tolman, H., 1994. Wind waves and movable-bed bottom friction. *Journal of Physical Oceanography*, 24: pp. 994–1009, ([http://dx.doi.org/10.1175/1520-0485\(1994\)0240994:WWAMB2.0.CO;2](http://dx.doi.org/10.1175/1520-0485(1994)0240994:WWAMB2.0.CO;2)).
- Weitzman, J.S., Zeller, R.B., Thomas, F.I.M., Koseff, J.R., 2015. The attenuation of current- and wave-driven flow within submerged multispecific vegetative canopies. *Limnol. Oceanogr.* 60 (6), 1855–1874. <http://dx.doi.org/10.1002/lno.10121>.
- Welch, P.D., 1967. The use of fast Fourier transform for the estimation of power spectra: a method based on time averaging over short, modified periodograms. *I. E. E. E. Trans. Audio Electro.* 15 (2), 70–73. <http://dx.doi.org/10.1109/TAU.1967.1161901>.
- Young, B.M., Harvey, L.E., 1996. A spatial analysis of the relationship between mangrove (*avicennia marina* var. *australasica*) physiognomy and sediment accretion in the hauraki plains, New Zealand. *Estuarine, Coastal and Shelf Science*, 42: pp. 231–246, (<https://doi.org/10.1006/ecss.1996.0017>).
- Zeller, R.B., Zarama, F.J., Weitzman, J.S., Koseff, J.R., 2015. A simple and practical model for combined wave-current canopy flows. *J. Fluid Mech.* 767, 842–880. <http://dx.doi.org/10.1017/jfm.2015.59>.